Article

Not peer-reviewed version

Harmaline and Human ClpP Activation for Pediatric Diffuse Intrinsic Pontine Glioma (DIPG) Treatment

Morena Miciaccia , Francesca Rizzo , Antonella Centonze , Gianfranco Cavallaro , Marialessandra Contino , Domenico Armenise , Olga Maria Baldelli , Roberta Solidoro , Savina Ferorelli , Pasquale Scarcia , Gennaro Agrimi , Veronica Zingales , Elisa Cimetta , Simone Ronsisvalle , Federica Maria Sipala , Paola Loguercio Polosa , Cosimo Gianluca Fortuna , Maria Grazia Perrone * , Antonio Scilimati

Posted Date: 22 December 2023

doi: 10.20944/preprints202312.1709.v1

Keywords: Harmaline; hClpP activation; DIPG; Molecular modeling

Article

Harmaline and Human ClpP Activation for Pediatric Diffuse Intrinsic Pontine Glioma (DIPG) Treatment

Morena Miciaccia [1,§], Francesca Rizzo [2,§], Antonella Centonze [1,§], Gianfranco Cavallaro [3], Marialessandra Contino [4], Domenico Armenise [1], Olga Maria Baldelli [1], Roberta Solidoro [1], Savina Ferorelli [1], Pasquale Scarcia [2], Gennaro Agrimi [2], Veronica Zingales [5], Elisa Cimetta [5], Simone Ronsisvalle [6], Federica Maria Sipala [6], Paola Loguercio Polosa [2], Cosimo Gianluca Fortuna [3,*], Maria Grazia Perrone [1,*] and Antonio Scilimati [1,*]

[1] Research Laboratory for Woman and Child Health, Department of Pharmacy - Pharmaceutical Sciences, University of Bari "Aldo Moro", Via E. Orabona 4, 70125, Bari, Italy; morena.miciaccia@uniba.it (M.M.); antonella.centonze1@uniba.it (A.C.); domenico.armenise1@uniba.it (D.A.); olga.baldelli@uniba.it (O.M.B.); roberta.solidoro@uniba.it (R.S.); savina.ferorelli@uniba.it (S.F.); mariagrazia.perrone@uniba.it (M.G.P.); antonio.scilimati@uniba.it (A.S.).

[2] Department of Biosciences, Biotechnologies, and Environment, University of Bari "Aldo Moro", Via E. Orabona 4, 70125 Bari, Italy; francesca.rizzo1@uniba.it (F.R.); pasquale.scarcia@uniba.it (P.S.); gennaro.agrimi@uniba.it (G.A.); paolaannamaria.loguerciopolosa@uniba.it (P.L.P.).

[3] Laboratory of Molecular modelling and Heterocyclic compounds ModHet, Department of Chemical Sciences, University of Catania, Viale Andrea Doria 6, 95125 Catania, Italy; gianfrancocav9234@gmail.com (G.C.); cg.fortuna@unict.it (C.G.F.).

[4] Department of Pharmacy - Pharmaceutical Sciences, University of Bari "Aldo Moro", Via E. Orabona 4, 70125, Bari, Italy; marialessandra.contino@uniba.it (M.C.).

[5] Department of Industrial Engineering (DII), University of Padua, Via Marzolo 9, 35131 Padova, Italy; veronica.zingales@uv.es (V.Z.); elisa.cimetta@unipd.it (E.C.).

[6] Department of Drug and Health Sciences, University of Catania, Viale Andrea Doria 6, 95125 Catania, Italy; s.ronsisvalle@unict.it (S.R.); federica.sipala@phd.unict.it (F.S.).

* Correspondence: mariagrazia.perrone@uniba.it (M.G.P.); antonio.scilimati@uniba.it (A.S.); cg.fortuna@unict.it (C.G.F.).

§ The authors contributed equally to this study and must be considered co-first names: morena.miciaccia@uniba.it(M.M.); francesca.rizzo1@uniba.it (F.R.); antonella.centonze1@uniba.it (A.C.).

Abstract: Diffuse intrinsic pontine glioma (DIPG), affecting children aged 4-7 years, is a rare, aggressive tumor that originates in the pons and then spreads to nearby tissue. DIPG is the leading cause of death for pediatric brain tumors due to its infiltrative nature and inoperability. Radiotherapy has only a palliative effect in stabilizing symptoms. *In silico* and preclinical studies identified ONC201, as a cytotoxic agent against some human cancer cell lines, including DIPG ones. Single crystal X-ray analysis of the complex of the human mitochondrial caseinolytic serine protease type C (*h*ClpP) and ONC201 (PDB ID: 6DL7) allowed to identify *h*ClpP as its main target. Hyperactivation of *h*ClpP causes damage to mitochondrial oxidative phosphorylation and cell death. In some DIPG patients, receiving ONC201, an acquired resistance was observed. In this context, a wide program initiated to discover original scaffolds for new *h*ClpP activators to treat ONC201-non-responding patients. Harmaline, a small molecule belonging to the chemical class of β -carboline, was identified through Fingerprints for Ligands and Proteins (FLAP), a structure-based Virtual Screening approach. Molecular dynamics simulations and a deep *in vitro* investigation showed interesting information on the interaction and activation of *h*ClpP by harmaline.

Keywords: harmaline; *h*ClpP activation; DIPG; molecular modeling

Preprints (www.preprints.org) | NOT PEER-REVIEWED | Posted: 22 December 2023 doi:10.20944/preprints202312.1709.v1

1. Introduction

Diffuse intrinsic pontine glioma (DIPG), primarily occurring in children [1], is a high-grade glioma (HGG) belonging to the category of diffuse midline glioma (DMG), as recently classified by WHO [2].

DIPG is the most common brainstem tumor in children, accounting for approximately 75-80% of all cases; 150-300 patients are diagnosed with DIPG in the USA per year, and a similar number occurs in Europe. The median age of patients with DIPG is approximately 4-7 years (Figure 1A). No gender difference has been observed among DIPG patients [2].

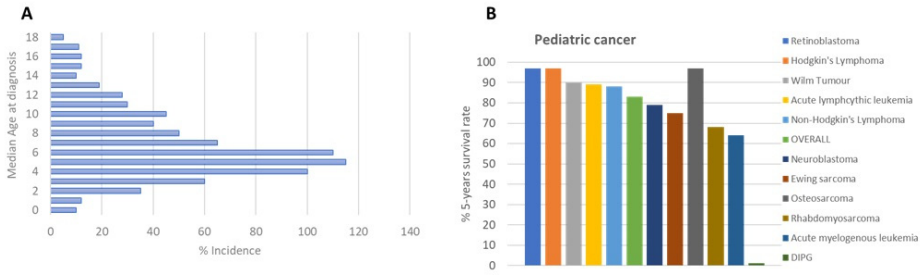

Figure 1. (a) Age of DIPG patients at diagnosis; **(b)** DIPG 5-years survival rate [https://www.dipg.org/dipg-stats].

DIPG clinical treatment, like many other diseases, is borrowed from adults, with unsuccessful results despite extensive research efforts made in the field, as indicated by hundreds of publications, with more than 500 paper in the last six years. Radiation therapy is the first-line treatment of DIPG patients with a survival benefit of only 3 months [3] (Figure 1B), transiently improving neurological deficits.

Most of research on DIPG is performed with ONC201 (Figure 2A), an imipridone, which has raised hopes as its use in the treatment of glioblastomas of bevacizumab-resistant adults led to an increase in overall survival (OS) and in some cases regression of the primary thalamic lesion [4].

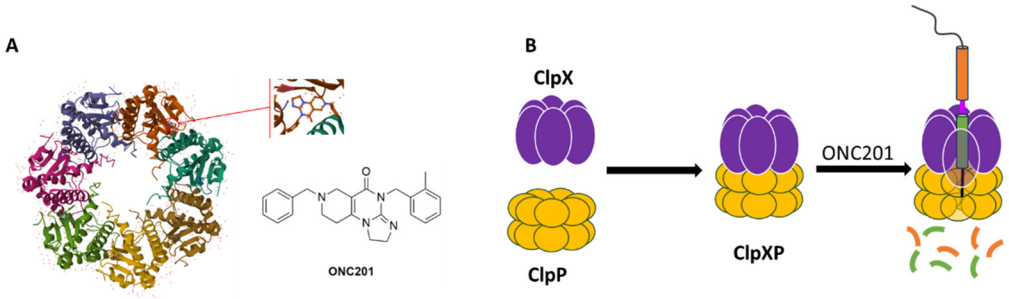

Figure 2. (a) Chemical structure of ONC201 and horizontal view of the complex between ONC201 and *h*ClpP (Adapted from PDB ID: 6DL7); **(b)** Structure of the ClpXP complex.

In May 2019, the diffractometric characterization (single crystal X-ray) of the complex between the human mitochondrial caseinolytic serin-protease P (*h*ClpP) and ONC201 (PDB ID: 6DL7) (Figure 2A) led to the identification of this enzyme as its main ONC201biological target [5].

*h*ClpP is part of a ClpXP mitochondrial matrix cylinder-shaped complex (*h*ClpP serine protease and the ATP-dependent proteases (AAA+ proteases) ClpX), which is an ATP-dependent protease that mediates the active remodeling, unfolding, and degradation of mitochondrial proteins using energy derived from ATP (Figure 2B). AAA+ proteases identify misfolded or damaged proteins in mitochondria [6]. Changes in cellular metabolism and bioenergetics, oxidative stress, and intracellular level of ROS are hallmarks of cancer development, these proteases are also important for the proliferation and metastasis of some types of cancers [7].

Preprints (www.preprints.org) | NOT PEER-REVIEWED | Posted: 22 December 2023 doi:10.20944/preprints202312.1709.v1

Both genetic and chemical inhibition of ClpXP and its overactivation by chemical and mutation cause the tumor cell death. In fact, on the one hand, inhibition leads to the accumulation of misfolded and damaged respiratory chain proteins and impairs oxidative phosphorylation, resulting in the selective death of cancer cells [8]. Inhibitors of *h*ClpP covalently modify the fourteen catalytic residues of Ser153 located within the lumen of the *h*ClpP tetradecamer [9]. Several inhibitors of *h*ClpP have been developed, and their chemical structures optimized. Beta-lactones were initially developed as antibiotics to treat *Staphylococcus aureus* infections. A2-32-01 (Figure 3) also showed cytotoxicity in leukemic cell lines, osteosarcoma cell line 143B, and primary leukemic cells over-expressing *h*ClpP [7, 10]. Despite the positive results in *in vitro* tests, the reduced plasma stability due to the easy lactone hydrolysis and their poor selectivity limited the corresponding clinical development [11].

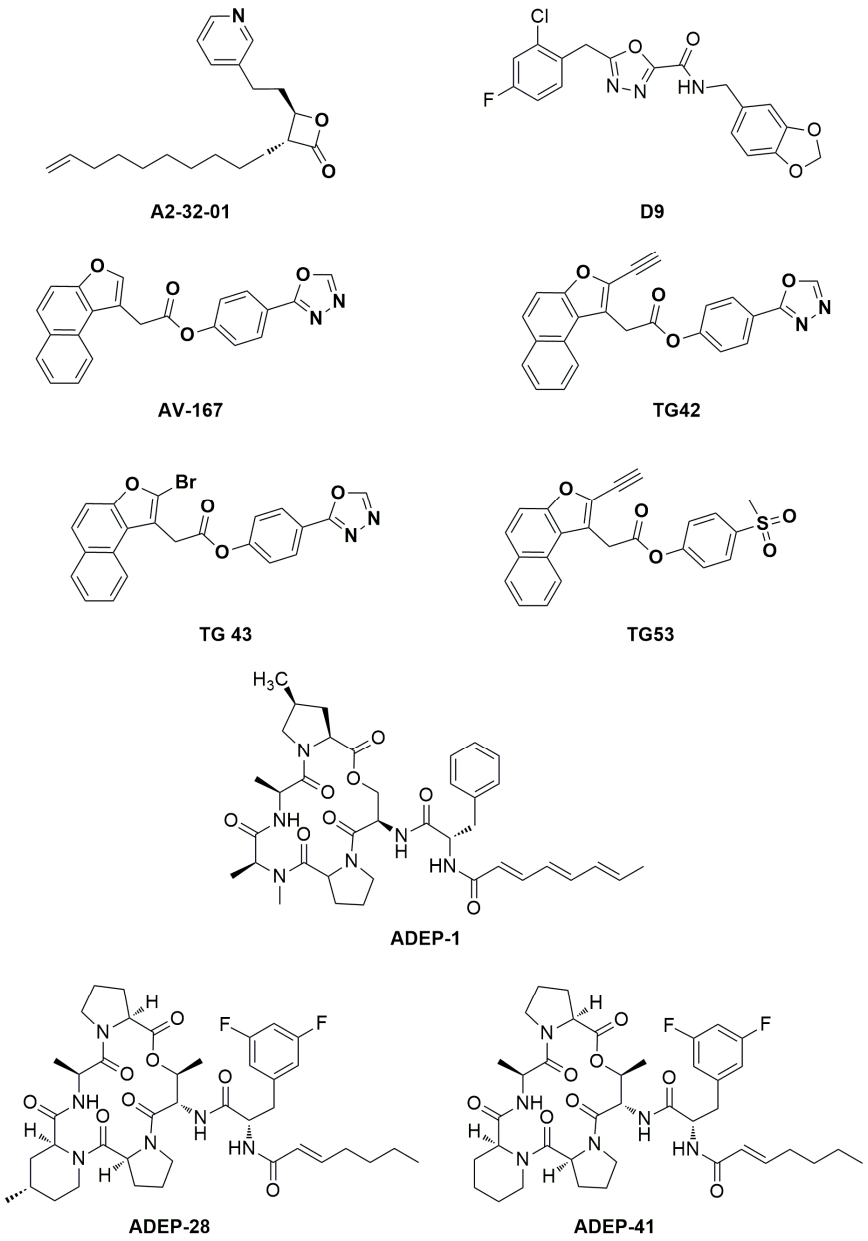

Figure 3. Chemical structure of *h*ClpP inhibitors and inducers.

The phenyl esters AV-167, TG42, TG43, and TG53 (Figure 3) developed to improve the chemical stability and potency of β-lactones, exhibited off- and on-target effects that blocked any further study [9].

Over-activation of *h*ClpP by its activators results in mitochondrial morphological damage and a decrease in oxidative phosphorylation, inducing tumor cell death [8]. Therefore, targeting AAA+

 doi:10.20944/preprints202312.1709.v1

proteases like ClpXP could be a strategy against malignant cells sparing normal tissues. Activators binding to the allosteric *h*ClpP site, produce conformational changes in the enzyme complex, resulting in the enlargement of the axial proteolytic pore and compaction of the protease. These changes lead to *h*ClpP hyperactivation and increase substrate degradation in a selective and uncontrolled manner [8]. To date, it is not known whether inhibition or activation of *h*ClpP would be the preferred therapeutic strategy.

Three classes of *h*ClpP activators are known: 1) acyldepsipeptides [ADEPs: representative members of ADEPs are ADEP-1, ADEP-28 and ADEP-41 (Figure 3)] are antibiotics that bind to hydrophobic pockets present between neighboring *h*ClpP subunits, which usually bind the IGF loop of ClpX, inducing enlargement of the axial pore and structuring of the axial *h*ClpP loop, resulting in unregulated entry and protein degradation [12, 13]; 2) oxadiazocarboxyamides, like D9 (Figure 3), whose binding induces dissociation of the ClpXP complex, and stabilization of the *h*ClpP activated state by widening the axial pore of the protease [14]; 3) imipridones, like ONC201, activate *h*ClpP in a dose-dependent manner as ADEP and D9 [15]. ONC201 binds noncovalently to the hydrophobic allosteric pockets present between neighboring subunits of *h*ClpP. Specifically, ONC201 binding induces *h*ClpP axial pore enlargement, while the complex adopts a more compact conformation like that induced by the binding of ADEP and D9 [16].

Despite ONC201 rapid development, its pharmacokinetic and pharmacodynamic profile needs to be improved. In fact, the doses used in clinical trials are very high, not all patients respond to the treatment, and its antipsychotic effects should also be considered, as it acts as a Dopamine D2 receptor (DRD2) antagonist [17].

Herein, a drug repurposing study is described. It was accomplished starting by an *in silico* investigation using ~1500 natural products already on the market with other therapeutic indications, aimed at identifying a novel original scaffold to be used to build more performant *h*ClpP activators. Harmaline was identified by a structure-based Virtual Screening study using Fingerprints for Ligands and Proteins (FLAP). It was tested as a *h*ClpP activator, cytotoxic compound on two representative DIPG cell lines (SU-DIPG-36 and SU-DIPG-50) and spheroids of mitochondrial SH-SY-5Y and SK-N-AS, and efflux pump substrate or modulator. Molecular dynamic experiments were used to explain the obtained results.

2. Materials and Methods

2.1. Computational studies

A database of NPs was downloaded from INDOFINE Chemical Company (https://indofinechemical.com) and SPECS libraries (https://www.specs.net/index.php). This Database consists of 1,536 natural compounds, 1489 from SPECS library and 47 from INDOFINE; these are all commercially easily available. They are NPs reflected in the pharmaceutical industry and have a specific activity. The in-silico evaluation (PLS analysis) of the database was carried out using Volsurf+ (VS+) software. Virtual screenings were performed through FLAP software in Structure-based mode (SBVS) [18]. The software identifies the interaction fields (MIFs), calculated in GRID, which represent the interactions between the molecules under examination and the areas of interest (called pockets) identified within the crystalline structure [18-19]. GRID MIFs were generated using four molecular probes: H (shape, steric effects), DRY (hydrophobic interactions), N1 (H-bond donor), and O (H-bond acceptor) interactions. In addition, SBVS mode returns three other important scores for evaluating interactions: GLOB-SUM, GLOB-PROD, and Distance. The first two values refer to the summation and production of the interactions, respectively. The Distance score represents the overall similarity derived from a combination of the degree of overlap between the individual probes (H, DRY, O, and N1) of the MIFs calculated for each candidate ligand and binding site. The crystallized structure used on FLAP is *h*ClpP in complex with ONC201 (PDB code: 6DL7 resolution 2.00 Å). The GLOB-SUM score was used as a reference to evaluate the degree of interaction. The GLOB-PROD is not used because it is not very indicative; it could be influenced by interaction scores with zero values.

 doi:10.20944/preprints202312.1709.v1

Molecular dynamics simulations were conducted using the optimal poses for harmaline and ONC201 within the pocket. Molecular dynamics studies were performed using Flare software version 6 (Cresset®, Litlington, Cambridgeshire, UK) [20-21].

The structures of the ligands were obtained from molecular docking studies and subsequently optimized using the software function "Flare preparation ligand" to minimize their energy. Protein preparation was performed using the "ProteinPrep" function of the software. This tool allows for the automated preparation of proteins for docking and molecular dynamics simulations. A TIP3P waterbox was produced, and the complexity was minimized. The force field used for proteins was AMBER FF14SB, and AMBER GAFF2 was used for the ligands [22-23].

Three simulations were conducted over a period of 10 ns. The root-mean-square deviation (RMSD) evaluation at the 10 ns mark revealed no significant variations. The Flare 6.0 software was employed to visualize and examine the molecular dynamics simulations. Furthermore, the WaterSwap absolute binding free energy method was utilized to determine the binding free energies of the ligand-protein complexes investigated, employing a function available in Flare software. The binding free energy was calculated using Bennett's method, thermodynamic integration (TI), and free energy perturbation (FEP). The binding free energy values were obtained by calculating the arithmetic mean of the energies determined using these methods.

2.2. Biochemical studies. Plasmid construction, hClpP expression, and affinity purification

To obtain the *h*ClpP construct suitable for protein expression, the cDNA was engineered by PCR. *h*ClpP cDNA (GenBank accession no. Z50853.1) coding sequence was deprived of the first 57 amino acids [24] corresponding to the mitochondrial targeting sequence MTS, and the ATG codon of the initiating methionine was added. At the 3' end of the coding sequence, the TEV cleavage site, a V5 epitope, and a 6xHis tag were added [43-44], followed by a stop codon (Table 1). The construct was cloned into the isopropyl-1-thio-B-D-galactopyranoside (IPTG)-inducible expression vector pET-21b. The *h*ClpP/pET recombinant plasmid was transformed into E. coli BL21-CodonPlus (DE3)-RIL competent cells (Stratagene); plasmid DNA was isolated from positive clones, and the insert was verified by DNA sequencing. The amino acid sequence is shown in Table 1.

Table 1. *h*ClpP amino acid sequence.

MPLIPIVVEQTGRGERAYDIYSRLLRERIVCVMGPIDDSVASLVIAQLLFLQSESNKKPIHMYINSPG
GVVTAGLAIYDTMQYILNPICTWCVGQAASMGSLLLAAGTPGMRHSLPNSRIMIHQPSGGARGQA
TDIAIQAEEIMKLKKQLYNIYAKHTKQSLQVIESAMERDRYMSPMEAQEFGILDKVLVHPPQDGE
DEPTLVQKEPVEAAPAAEPVPAST**ENLYFQG**KL**GKPIPNPLLGLDST**RTG**HHHHHH**

TEV sequence	**ENLYFQG**
V5 epitope	**GKPIPNPLLGLDST**
His Tag	**HHHHHH**

The recombinant protein was expressed in *E. coli* BL21-Codon Plus (DE3)-RIL cells. Briefly, a log-phase 250-ml culture (OD600 ~ 0.6), grown in Luria-Bertrani Broth (LB; 10 g/L tryptone, 5 g/L yeast extract, 10 g/L NaCl) supplemented with 0.1 mg/ml ampicillin, was induced with 0.5 mM Isopropil-β-D-1-tiogalattopiranoside (IPTG, Sigma) for 3 h at 22 °C with shaking at 260 rpm.

Bacteria were harvested by centrifugation at 4,600 g for 15 min at +4 °C; pellets were washed with cold PBS and either immediately processed for protein extraction or fast frozen in liquid nitrogen and stored at -80°C. To disrupt bacteria, pellets were resuspended in 25 ml of Lysis/binding buffer (25 mM Tris/HCl pH 7,8, 150 mM NaCl, 10% glycerol, 5 mM imidazole); the mixture was added with 1mg/ml of freshly prepared lysozyme (Sigma) in 10 mM Tris/HCl pH 8.0 and incubated on ice for 30 min with occasional swirling. Cells were sonicated on ice/water with Vibracell Sonics (large probe), 30-sec pulse, 30-sec pause, amplitude 40% for ~ 60 min. Protein purification was achieved by immobilized metal ion affinity chromatography (IMAC) using a Ni-NTA prepacked column. After

Preprints (www.preprints.org) | NOT PEER-REVIEWED | Posted: 22 December 2023 doi:10.20944/preprints202312.1709.v1

cell disruption, the cell lysate was cleared by ultracentrifugation at 100,000 g or, alternatively, by filtering through a 0.4 µm membrane. The NaCl concentration in all buffers was low (150 mM) in order to preserve the double heptamer ring of the oligomeric *h*ClpP complex and, with it, the enzymatic activity. The S100 was passed through the IMAC column and extensive washing was performed to remove most of the impurities, while the recombinant *h*ClpP protein remained bound due to the high affinity of the 6xHis tag. To improve *h*ClpP purification two step elutions were applied, one with a buffer containing 50 mM imidazole, which removed most of the *E. coli* contaminating proteins, and the other at 300 mM imidazole to elute the specifically bound protein. Identification of *h*ClpP in the eluted fractions was performed by SDS-PAGE / western blot analysis using a monoclonal antiserum against recombinant *h*ClpP. As shown in Figure 4A, all eluted fractions revealed immunopositive bands. A typical profile of specific affinity elution was obtained in the fractions eluted at 300 mM imidazole. In particular, fractions 7-10 showed several bands, two of which migrated with an apparent molecular mass between ~34 kDa and ~30 kDa. The calculated mass value for the recombinant *h*ClpP is 27.9 kDa, which is closer to the apparent size of the faster migrating band (asterisk). The slower migrating bands, which are more evident in fraction n° 8, could be likely caused by atypical forms of SDS-polypeptide complexes and/or partially denatured proteins, which often occur during gel separation [27-28]. Interestingly, a higher electrophoretic mobility for the human recombinant *h*ClpP separated by SDS-PAGE was also reported [29]. Fraction n° 8 from 300 mM imidazole elution, which was highly enriched in *h*ClpP, was also subjected to native PAGE. The *h*ClpP protein was revealed by western blot analysis, showing three major bands (Figure 4B). Although it is difficult to predict the apparent molecular mass of the bands, however one could speculate that the band migrating as ~ 250 kDa (asterisk) might represent the heptamer ring. This would be in line with the finding that *h*ClpP expressed in *E. coli* forms a stable heptamer [30]. The bands with a higher apparent molecular mass could likely correspond to different oligomeric complexes, including the tetradecamer that is the enzymatic active form.

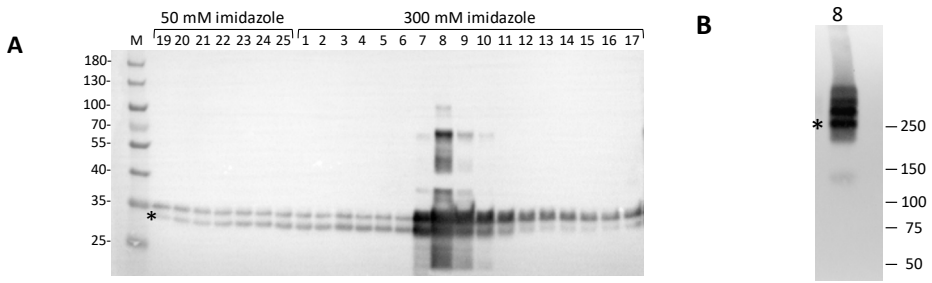

Figure 4. Western blot analysis of Ni-NTA eluted fractions**. (a)** Fractions eluted at 50 mM and 300 mM imidazole buffer were resolved on a 4-12% denaturing polyacrylamide gel (Bio-Rad Criterion XT Bis-Tris) in MOPS 1X buffer and blotted onto PVDF membrane for western blotting. 5-µl sample of each fraction was loaded. Marker (M): PageRuler Prestained Protein Ladder (Thermo). *h*ClpP specific bands were visualized by immunoreaction with polyclonal antiserum against *h*ClpP (1:20000, Abcam, ab124822); **(b)** Native PAGE/Western blotting of fraction n° 8 from the IMAC chromatography. 5 µl sample were separated on a 4-15% protein gel (Bio-Rad Mini-PROTEAN TGX) in TGX 1X buffer. The positions and molecular masses of co-electrophoresed marker proteins are shown on the left (Precision Plus Dual Color Marker, Bio-Rad).

For SDS-PAGE, column fractions (5 µl) were solubilized in 1x Laemmli buffer (Bio-Rad) and separated on a 4-12% denaturing polyacrylamide gel (Bio-Rad Criterion XT Bis-Tris) in MOPS 1X buffer. For native PAGE, a 5-µl volume of the indicated fraction was solubilized in 6X Native protein loading buffer (600mM TrisHCl pH 6.8, 50% Glycerol, 0.02% Bromophenol blue without DTT) and separated on a 4-15% protein gel (Bio-Rad Mini-PROTEAN TGX) in TGX 1X buffer. For western blotting, proteins in the gel were electrotransferred onto polyvinylidene difluoride (PVDF) membranes (Immobilion-P PVDF Membrane 0.45µm) at +4°C for 3 h. Immunoblotting was performed according to standard techniques. The primary antibody was from Abcam; detection was

 doi:10.20944/preprints202312.1709.v1

performed with the HRP-conjugated secondary antibody (Bio-Rad). Chemiluminescent detection was achieved using Amersham ECL™PrimeWestern blotting detection reagent (GE Healthcare Life Sciences, Marlborough, MA, USA) or ClarityWestern ECL substrate (Bio-Rad, Hercules, CA, USA); signals were revealed by ChemiDoc MP Imaging System (Bio-Rad, Hercules, CA, USA). Fractions containing *h*ClpP were stored on ice in the cold room for 24 hours for the fluorogenic assay.

2.3. hClpP activity test

To assess the potency of the proteolytic activity of *h*ClpP, a FITC-Casein assay was performed. In a black flat bottom 96-well plate, a 3 µM solution of purified *h*ClpP in Assay Buffer (50 mM HEPES, pH 7.5, 300mM KCl, 1mM DTT, 15%v/v glycerol; AB) preincubated at 37°c for 15 min was added to 5 µL of tested compounds in DMSO at different concentrations (ranging from 1 to 100 µM) and incubated for 15 min at 37°C under shaking. As a control, three wells were filled with 5 µL DMSO. Kinetic measurement was started after adding 2 µM of the fluorogenic peptides FITC-Casein (Merck, C3777), used as a hydrolytic substrate. Fluorescence of the cleaved FITC was recorded over 60 min at 37 °C on a Tecan Infinite M200 pro (λex: 485 nm, emission λem: 535 nm, gain 60). The slope in linear range between 600-1800s was determined and plotted against time. EC_{50} for each tested compound was calculated using GraphPad Prism 7.05. Results are reported as the mean of two independent experiments performed in triplicate.

2.4. Cell cultures

Patient-derived diffuse intrinsic pontine glioma (DIPG) cell cultures (SU-DIPG-36, SU-DIPG-50) were provided and previously characterized by Dr Michelle Monje with the approval of the Institutional Review Board (Stanford University). These cells were maintained as a monolayer in Tumor Stem Media (TSM) consisting of 1:1 mixture of DMEM /F12 (Invitrogen) and Neurobasal (-A) (Invitrogen), supplemented with B27 (-A) (Life Technologies), human basic fibroblast growth factor (bFGF) (20 ng/ml) (Life Technologies), recombinant human epidermal growth factor (EGF) (20 ng/ml) (Life Technologies), platelet-derived growth factor-AA (PDGF-AA, 10 ng/mL), PDGF-BB (10 ng/ mL) (Life Technologies) and heparin (20 ng/ml) (StemCell Technologies) at 37°C in 5% CO_2 (media change once a week) [31-33].

Caco-2 cells were grown in Dulbecco's Modified Eagle Medium high glucose (DMEM high glucose, Euroclone S.p.A., Pero, MI, Italy) supplemented with 10% Fetal Bovine Serum (FBS, Euroclone S.p.A., Pero, MI, Italy), 2 mM glutamine (Euroclone S.p.A., Pero, MI, Italy), 100 U/mL penicillin and 0.1 mg/mL streptomycin (Euroclone S.p.A., Pero, MI, Italy). MDCK-BCRP cells are from Prof. P. Borst, NKI-AVL Institute, Amsterdam. MDCK cells were grown in DMEM high glucose supplemented with 10% fetal bovine serum, 2 mM glutamine, 100 U/mL penicillin, 100 µg/mL streptomycin, in a humidified incubator at 37 °C with a 5 % CO_2 atmosphere. Human neuroblastoma SH-SY5Y (ATCC-CRL-2266, MYCN not amplified) and SK-N-AS (ATCC CRL-2137, MYCN not amplified) cells (from Prof. E. Cimetta, Istituto di Ricerca Pediatrica Citta' della Speranza, Padova, Italy) were cultured in monolayer in DMEM high glucose with L-glutamine medium supplemented with 10% FBS, 1% MEM NEAA (100X) and 1% penicillin/streptomycin. Cells were grown at pH 7.4, 5% CO_2 at 37 ◦C and 95% air atmosphere at constant humidity. The medium was replaced every 2–3 days. To obtain a single, centred, and highly reproducible spheroid per well, ultra-low attachment (ULA, Sarstedt®) 96-well round bottom plates were used. The 3D spheroid cultures were generated from single-cell suspensions obtained from trypsinized monolayers of both cell lines. Then, 200 µl of cell suspension (2 × 103 cells) were seeded into each well of the plates. Each plate was centrifuged at 1,200 rpm for 5 min to help cells settle rapidly to the bottom of the wells. Each spheroid for both cell lines measured approximately 500 µm in diameter.

3D spheroids growth and morphology were monitored for seven days regarding changes in volume and shape. Bright-field microscope images and morphological analyses of spheroids were carried out with the inverted light microscope Zeiss Primo Vert equipped with a Zeiss camera (Axiocam 208 color, Zeiss Microscopy, Germany) at 10× magnification. The software Zen Lite version 2.6 (Zeiss Microscopy, Germany) was used to achieve morphological parameters (diameter and area).

 doi:10.20944/preprints202312.1709.v1

2.5.2. D Cell viability Assay

Determination of cell growth was performed using the CCK8 assay at 72 h. On day 1, 10,000 cells per well were seeded into 96-well plates at 100 µl. On day 2, 100 µL of different concentrations (ranging from 1 to 100 µM) of test compounds, solved in a culture medium, were added to monolayers and incubated in a humidified atmosphere with 5% CO_2 at 37°C. In all the experiments, the various drug solvents (EtOH, DMSO) were added in each control to evaluate a possible solvent cytotoxicity. After incubation time with drugs, CCK8 (cat#96992 Sigma Aldrich, Milan, Italy) (10 µl) was added to each well, and after 3-4 h incubation at 37 °C, the absorbance values at λ=450 nm were determined on the Tecan Infinite 200 Microplate Reader. Using the GraphPad Prism, the IC_{50} for each drug treatment and for each cell line used was determined. Results are reported as the mean of two independent experiments performed in triplicate.

2.6.3. D cell viability assay

SH-SY5Y and SK-N-AS cultures were exposed to drugs on day 7 after spheroids formation, by replacing 100 µl of culture medium with medium containing the different drugs to obtain final concentrations ranging from 12.5 to 100 µM. Appropriate controls containing the same amount of solvent (≤1% v/v) were included in each experiment. Intracellular ATP levels were measured using the CellTiter-Glo® 3D Luminescent Cell Viability Assay (Promega®, G968B, Milan, Italy) according to the manufacturer's protocols. At the end of the exposure time (72 h), 150 µl of the medium was removed from each well and 50 µl/well of CellTiter-Glo reagent was added. The content was vigorously mixed for 5 minutes to induce cell lysis and to effectively extract ATP from 3D microtissue spheroids. Then, the plate was incubated at room temperature for 25 min, protected from light. The supernatant was transferred to an opaque white flat bottom 96-counter-well plate and the luminescence was measured on a Tecan microplate reader.

2.7. Calcein-AM experiment

These experiments were carried out as reported by Contino et al. with minor modifications to measure the P-gp activity [34]. MDCK-MDR1 cell line (30,000 cells per well) were seeded into black CulturePlate 96/wells plate with 100 µL medium and allowed to become confluent overnight in a humidified atmosphere with 5% CO_2 at 37°C. 100 µL of different concentrations (ranging from 0.1 to 100 µM) of test compounds, solved in culture medium, were added to monolayers and incubated for 30 min in humidified atmosphere with 5% CO_2 at 37°C. Then, 100 µL of Calcein-AM, solved in Phosphate Buffered Saline (PBS) (final concentration of 2.5 µM), was added to all the wells and the plate was incubated for 30 min at 37 °C, 5% CO_2. Each well was washed 3x100µL ice-cold PBS, and saline buffer was added to each well, and the plate was read with Victor3 (PerkinElmer) at excitation and emission wavelengths of 485 nm and 535 nm, respectively. In these experimental conditions, Calcein cell accumulation was evaluated in the absence and presence of test compounds, and fluorescence basal level was estimated with untreated cells. In treated wells, fluorescence increase was measured, with respect to the basal level. EC_{50} values were determined by fitting the fluorescence increase percentage versus log[dose].

2.8. Hoechst 33342 experiment

These experiments were carried out as described by Contino et al. with minor modifications to measure the BCRP activity profile [34]. MDCK-BCRP cell line (30,000 cells per well) was seeded into black CulturePlate 96/wells plate with 100 µL medium and allowed to become confluent overnight in a humidified atmosphere with 5% CO_2 at 37°C. 100 µL of several concentrations (ranging from 0.1 to 100 µM) of test compounds, solubilized in culture medium, were added to monolayers, and the plate was incubated for 30 min at 37 °C, 5% CO_2. Hoechst 33342 was added in 100 µL of Phosphate Buffered Saline (PBS) to yield a final concentration of 8 µM to the 96-wells plate, and the plate was incubated for 30 min at 37 °C, 5% CO_2. The supernatants were drained, and the cells were fixed for 20 min under light protection using 100 µL per well of a 4% PFA solution. Each well was washed 3

 doi:10.20944/preprints202312.1709.v1

times with 100 µL ice-cold PBS and 100 µL saline buffer added to each well, and the plate was read with Victor3 (PerkinElmer) at excitation and emission wavelengths of 340/35 nm and 485/20 nm, respectively. In these experimental conditions, Hoechst 33342 accumulation was evaluated in the absence and presence of test compounds, and fluorescence basal level was estimated with untreated cells. In treated cells, fluorescence increase with respect to basal level was measured. EC_{50} values were determined by fitting the fluorescence increase percentage versus log[dose].

2.9. ATPlite assay

The MDCK-MDR1 cells were seeded into a 96-well plate in complete medium (100 µL) at a density of $2x10^4$ cells per well [34], and the plate was incubated overnight in a humidified atmosphere with 5% CO_2 at 37°C. The medium was removed, and a complete medium (100 µL) was added in the presence or absence of different concentrations of the test compounds. The plate was incubated for 2 h in a humidified atmosphere with 5% CO_2 at 37 °C. Mammalian cell lysis solution (50 µL) was added to all wells, and the plate was shaken for 5 min in an orbital shaker. Substrate solution (50 µL) was added to all wells, and the plate was shaken for 5 min in an orbital shaker. The plate was dark-adapted for 10 min, and the luminescence was measured in Victor3 (PerkinElmer).

2.10. Permeability experiments

Preparation of Caco-2 monolayer. Caco-2 cells were seeded onto a Millicell assay system (Millipore), in which a cell monolayer was set in between a filter cell and a receiver plate at a density of 20000 cells $well^{-1}$. The culture medium was replaced every 48 h, and the cells were kept for 21 days in culture. The trans-epithelial electrical resistance (TEER) of the monolayers was measured daily, before and after the experiment, by using an epithelial voltohmmeter (Millicell-ERS) [35]. Generally, TEER values greater than 1000 W for a 21-day culture are considered optimal.

2.11. Drug-transport experiment

After 21 days of Caco-2 cell growth, the medium was removed from the filter wells and the receiver plate, and they were filled with fresh Hank's balanced salt solution (HBSS) buffer (Invitrogen). This procedure was repeated twice, and the plates were incubated at 37 °C for 30 min. After the incubation time, the HBSS buffer was removed, and drug solutions and reference compounds were added to the filter well at a concentration of 100 mm, whereas fresh HBSS was added to the receiver plate. The plates were incubated at 37 °C for 120 min. Afterward, samples were removed from the apical (filter well) and basolateral (receiver plate) side of the monolayer to measure the permeability.

The apparent permeability (P_{app}), in units of nm s^{-1}, was calculated by using the following equation:

$$P_{app} = \frac{VA}{\text{area x time}} \times \frac{[drug]acceptor}{[drug]\ intial}$$

in which VA is the volume (in mL) in the acceptor well, the area is the surface area of the membrane (0.11 cm^2 of the well), time is the total transport time (7200 s), $[drug]_{acceptor}$ is the concentration of the drug measured by UV spectroscopy, and $[drug]_{initial}$ is the initial drug concentration ($1x10^{-4}$) in the apical or basolateral wells.

3. Results and Discussion

3.1. Computational Studies Based on the Fingerprints for Ligands and Proteins (FLAP) Algorithm

1,536 Natural Products (NPs) (*INDOFINE Chemical Company and SPECS libraries*) were subjected to an initial selection by Partial Least Square (PLS) analysis to predict their ability to cross the blood-brain barrier (BBB+). The entire database was projected onto a library model present in the software. According to Volsurf analysis, compounds BBB+ are in the blue area of the PLS region (Figure 5).

Preprints (www.preprints.org) | NOT PEER-REVIEWED | Posted: 22 December 2023 doi:10.20944/preprints202312.1709.v1

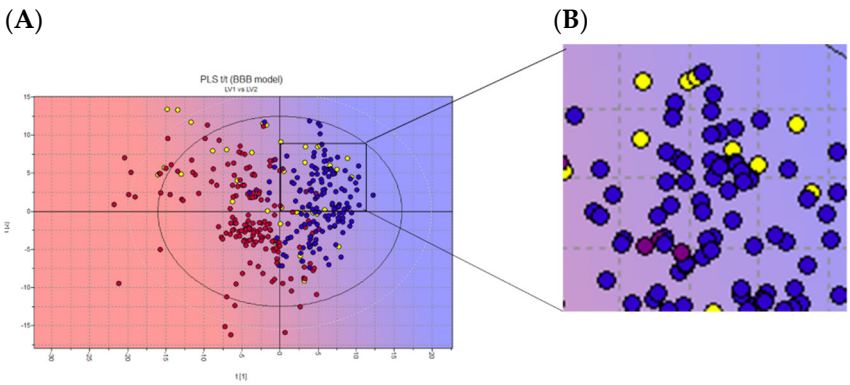

Figure 5. (a) 2D scores plot of the PLS activity model of BBB crossing. (**b**) Zoom on chosen NPs. Projected compounds are colored according to their BBB permeability: red for low BBB permeability and blue for high; yellow dots: NPs database. Representative image of the INDOFINE Chemical Company library only.

The selected ten NPs (yellow dots in the box, Figure 4) were subjected to a Structure-Based Virtual Screening (SBVS) based on the Fingerprints for Ligands and Proteins (FLAP) algorithm. SBVS was performed using the X-ray crystal structures of *h*ClpP in complex with ONC201 (PDB ID: 6DL7) [16]. FLAP identified 21 pockets, seven of which were identical (pockets 1 to 7) (Figure 6). These seven pockets are equivalently repeated in the seven monomer units of the crystal structure, and within each of them a molecule of ONC201 is present. Then, to study the interactions of *h*ClpP with the NPs under investigation, one of these seven pockets was randomly chosen.

After the removal of the co-crystallized ONC201, the ten NPs were examined by FLAP, and one of them, harmaline, showed an interaction score value similar to ONC201 (GLOB-SUM of 2.743 and 2.945, respectively). The respective 3D poses show similarities between the two compounds: the pocket area involved in the interaction is the upper one, and the two compounds are completely incorporated inside the pocket (Figure 6A-C). Similarities were also found in the 2D representation. Hydrophobic interactions (green areas) are the strongest in both cases, with small scattered areas of hydrogen bonding interactions (red and blue) (Figure 7B, 7D). The software highlights three redundant amino acid residues (Tyr118, Trp146, and Tyr138); which interact via hydrophobic interaction (π–π and CH–π) with the heterocycles. The compounds have similar structural features, such a condensed heterocycle, which may have affected the virtual projections with FLAP (very similar scores and poses).

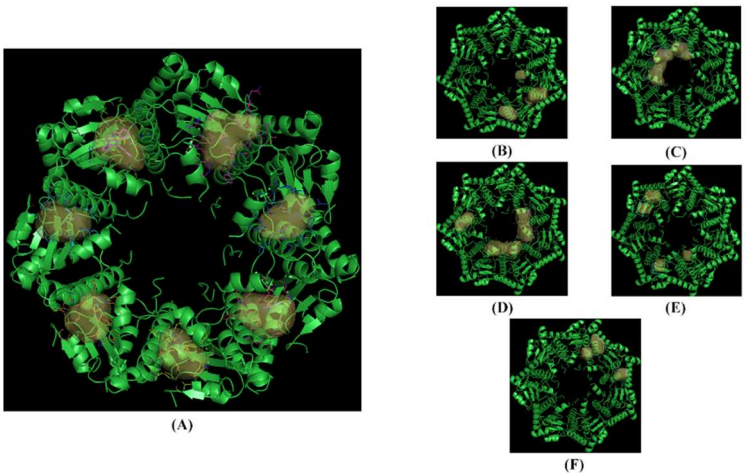

Figure 6. The crystallized structure and pockets of *h*ClpP: ONC201 complex. **(a)** Front view, pockets 1 to 7; **(b)** back view, pockets 8 to 10; **(c)** back view, pocket 11; **(d)** back view, pockets 12 to 14; **(e)** back view, pockets 15 to 18; **(f)** back view, pockets 19 to 21.

Preprints (www.preprints.org) | NOT PEER-REVIEWED | Posted: 22 December 2023 doi:10.20944/preprints202312.1709.v1

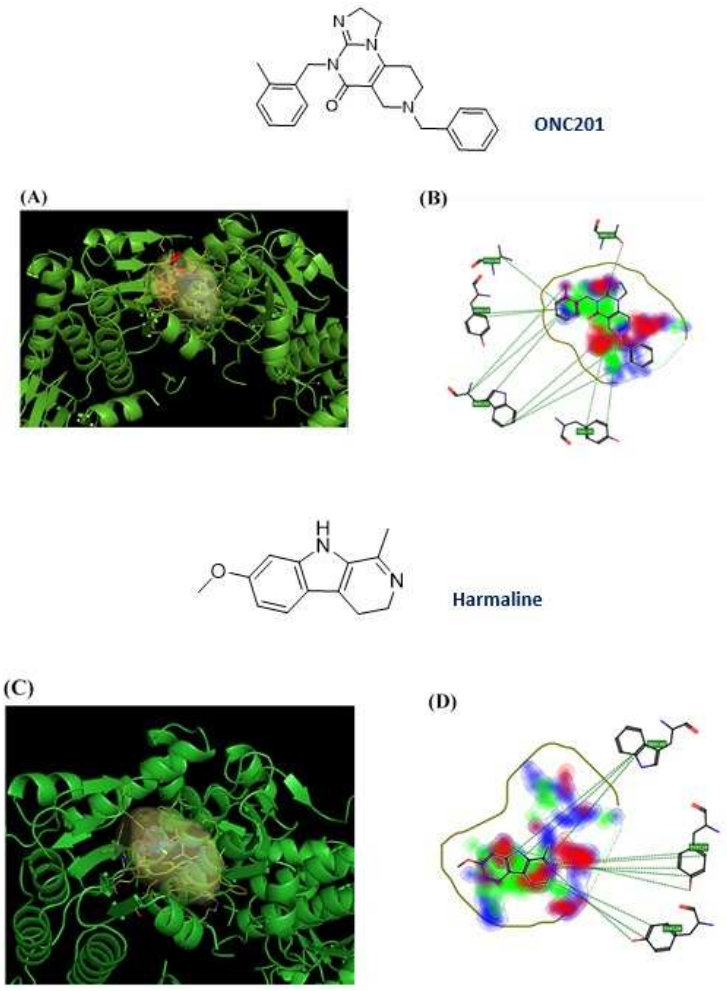

Figure 7. ONC201 and harmaline chemical structure and their 3D and 2D binding poses; **(a)** 3D binding poses for ONC201; **(b)** 2D binding pose for ONC201; **(c)** 3D binding poses for harmaline; **(d)** 2D binding poses for harmaline.

Harmaline (7-methoxy-1-methyl-4,9-dihydro-3*H*-pyrido[3,4-b]indole) is a naturally fluorescent (λ_{exc} = 330 nm; λ_{em} = 480 nm) [38] β-carboline alkaloid, isolated from *Peganum harmala L.*, with a tricyclic pyrido[3,4-b]indole ring structure. It is the partially hydrogenated form of harmine [39, 40].

Molecular dynamics studies have provided interesting results for harmaline. The molecule, characterized by its small structure and single rotatable bond, seeks stabilization during the initial nanoseconds of its dynamics, achieving a stabilized state during the final nanoseconds of the simulation, as illustrated in Figure 8a. In particular, the molecule endeavors to reach stability within the pocket for approximately 6 ns. Consequently, it forms hydrophobic (π–π) bonds with Tyr118, Tyr138, and Trp146, facilitated by the presence of three condensed rings. After approximately 8 ns, the molecule stabilizes in the selected pocket and moves slightly outward, while simultaneously maintaining its π–π interaction with Trp146 and forming a hydrogen bond with Tyr138.

On the other hand, dynamic simulations conducted on ONC201 (Figure 8b) revealed a good stability of the molecule within the pocket, with the formation of several hydrophobic interactions throughout the duration of the dynamics. It establishes π–π interactions with His116, Trp146, and Tyr138 throughout the duration of the simulation. Furthermore, the formation of a hydrogen bond with Tyr118 contributes to the stabilization of the molecule.

Preprints (www.preprints.org) | NOT PEER-REVIEWED | Posted: 22 December 2023 doi:10.20944/preprints202312.1709.v1

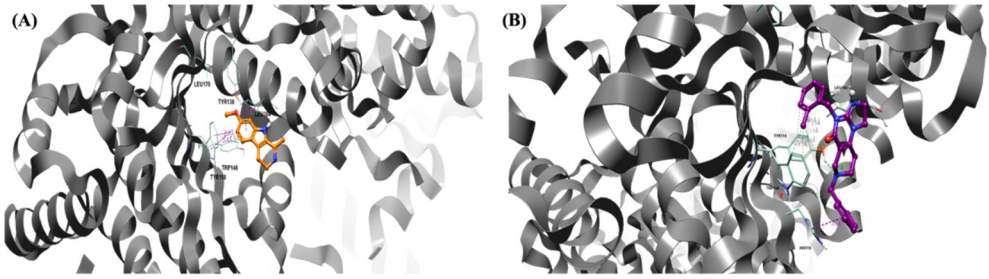

Figure 8. Pose of the two ligands in the pocket of *h*ClpP**.** Water and hydrogen were omitted for clarity. **(a):** Pose of Harmaline (orange) in the pocket of *h*ClpP. The frame was captured at 8.2 ns. **(b):** Pose of ONC201 (magenta) in the pocket of *h*ClpP. The frame was captured at 6.5 ns.

Overall, both molecules demonstrate stability within the pocket, which can be attributed to the diverse interactions they establish with the key amino acid residues proposed, Tyr118, Tyr138, and Trp146. Harmaline is characterized by three condensed rings and a reduced size compared with that of the reference molecule. This finding suggests that harmaline exhibits a reduced affinity for the examined pocket compared to ONC201 and displays notable but reduced stability.

As shown in Table 2, the binding free energies of ONC201 and harmaline obtained by Waterswap method are -33.27 ± 1.64 and -27.91 ± 1.87 respectively. The observations from the binding free energy values are consistent with the visualization of molecular dynamics simulations. Despite not demonstrating optimal free energy values, harmaline displays a sufficient binding affinity for *h*ClpP.

Table 2. Binding free energies of ONC201 and Harmaline with *h*ClpP calculated by Bennet, TI and FEP methods and relative consensus average.

Ligand	Bennet (kcal/mol)	FEP (kcal/mol)	TI (kcal/mol)	Consensus (kcal/mol)
Harmaline	-28.13	-28.08	-27.49	-27.91 ± 1.87
ONC201	-34.08	-32.51	-32.44	-33.27 ± 1.64

Harmaline has been extensively studied over the years for its broad pharmacological spectrum of activities. Indeed, besides its significant acetylcholinesterase (AChE) inhibitory activity with effects similar to the FDA-approved galantamine [41], it also inhibits the monoamine oxidase [42] and myeloperoxidase activity [43].

Harmaline also inhibits the cycloxygenase-2 activity, resulting in increased endocannabinoid (EC) levels in the brain and a concomitant reduction in stress and anxiety [44]. Among the numerous harmaline properties its use determines an improvement in learning and memory disorders induced in mouse models by scopolamine and ethanol [45]. It shows also antioxidant, anti-inflammatory, anti-tumor and anti-hypertensive effects [45]. Harmaline is cytotoxic in lung carcinoma cells by inhibiting sphingosine kinase-1/sphingosine-1-phosphate (SphK1), which is linked to cancer progression and survival of cells affected by chemotherapy [46]. It also induces anti-angiogenic effects in mouse models of breast cancer [47]. Furthermore, a very recent study also suggested harmaline as a promising candidate to treat Alzheimer's disease (AD) progression and neurodegeneration for its ability to inhibit microtubule affinity regulatory kinase 4 (MARK4), which is responsible for the development of cancer, diabetes, and neurodegenerative diseases [48] (Figure 9).

Preprints (www.preprints.org) | NOT PEER-REVIEWED | Posted: 22 December 2023 doi:10.20944/preprints202312.1709.v1

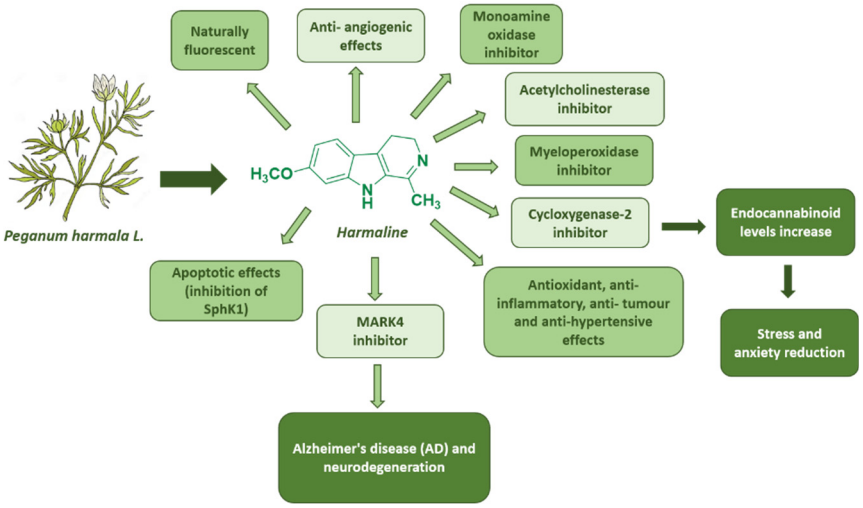

Figure 9. Summary of harmaline biological effects.

3.2. hClpP activation by harmaline and anticancer strategy

To evaluate the *h*ClpP activating potency of harmaline an *in vitro* FITC-Casein assay was performed. The mitochondrial *h*ClpP has been bacterially expressed, purified, and used to test three scalar concentrations of harmaline (1, 10, 100 µM). 28% activation of *h*ClpP was observed at the highest concentration, compared to 100 µM ONC201 used as a reference compound (Figure 10).

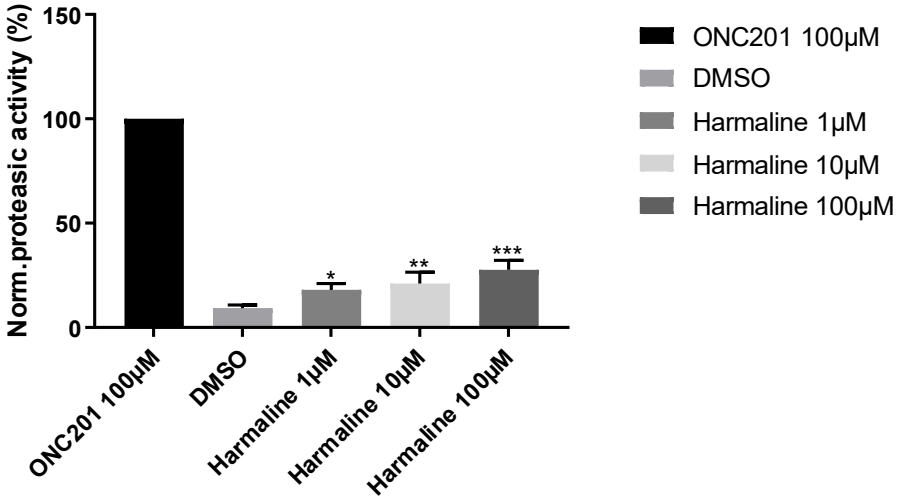

Figure 10. *h*ClpP induction by harmaline at different concentrations normalized to 100 µM ONC201 activity. DMSO was used as a control. Each bar represents the mean ± SEM of three experiments performed in triplicate. One-Way ANOVA vs. DMSO was applied and for * = $p < 0.05$; ** = $p < 0.01$; *** = $p < 0.0005$.

Some malignancies have specific mitochondrial characteristics that make them dependent on oxidative phosphorylation (OXPHOS) the fundamental mitochondrial process linking the tricarboxylic acid (TCA) cycle for the synthesis of cellular building blocks such as aspartate and increase ATP turnover. In these cases, OXPHOS is useful as a target to achieve a selective cytotoxic effect on malignant cells. Thus, targeting ClpP becomes an emerging anti-tumor strategy that takes advantage of the increased dependence of oxidative phosphorylation in these tumor types. Harmaline is known to exert its anti-tumor proprieties by modulating cellular and molecular mediators involved in cell cycle progression, cell proliferation, ROS balance, and apoptosis [49].

Preprints (www.preprints.org) | NOT PEER-REVIEWED | Posted: 22 December 2023 doi:10.20944/preprints202312.1709.v1

Therefore, cytotoxic activity of harmaline was evaluated on two H3K27M-altered cell cultures derived from DIPG patients, SU-DIPG-36, SU-DIPG-50 [50] and on neuroblastoma spheroids (SH-SY5Y and SK-N-AS).

Both DIPG cell lines have unamplified MYCN, a gene involved in tumor development and progression. Furthermore, SH-SY5Y is derived from a primary neuroblastoma, while SK-N-AS is from metastases [51-53].

After 72 hours exposure of SU-DIPG-36 and SU-DIPG-50 to 100 µM harmaline, the measured cancer cells death was 34 and 50%, respectively, compared to 100 µM ONC201, which shows a cytotoxic effect of 83 and 70% on the same cell lines, respectively (Figure 11).

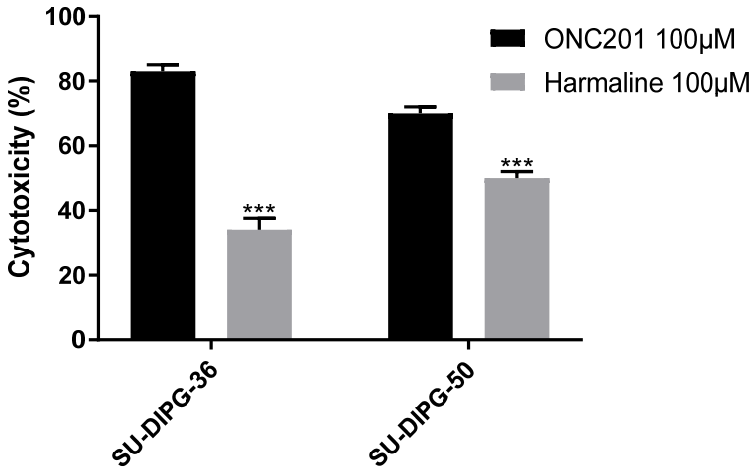

Figure 11. Cytotoxicity of 100 µM ONC201 and 100 µM harmaline on SU-DIPG-36 and SU-DIPG-50. Each bar represents the mean ± SEM of three experiments performed in triplicate. Two-Way ANOVA was applied, SU-DIPG-36: ONC201 vs. Harmaline p = 0.001, SU-DIPG-50: ONC201 vs. Harmaline p = 0.001.

The mitochondrial toxicity on neuroblastoma cell lines was evaluated by ATP assay after 72 hours exposure to different concentrations of compounds (12.5 – 100 µM) (Figure 12).

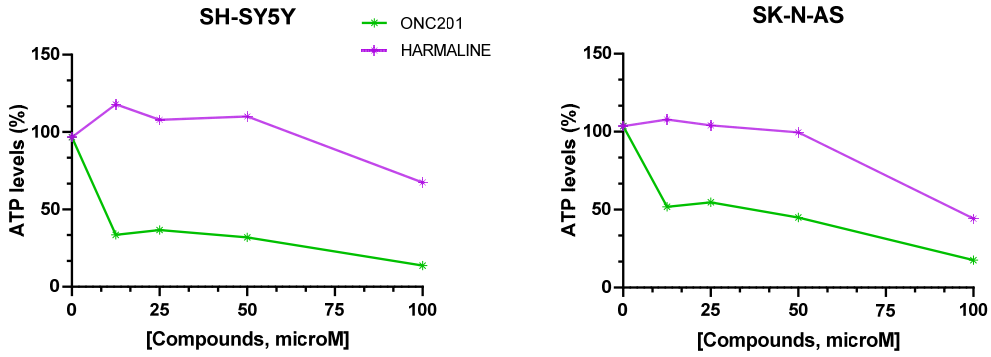

Figure 12. Percentage (%) ATP levels in SH-SY-5Y and SK-N-AS spheroids after 72 hours of drug exposure. Data are expressed as mean ± SEM of two independent experiments (n = 2).

For both cell lines, spheroids exposed to ONC201 revealed a decrease in cell viability of ~ 85%. (Table 2). The highest harmaline concentration led to a decrease in cell viability for SH-SY-5Y spheroids of ~32.5%, and of ~56% for SK-N-AS spheroids (Table 3).

Preprints (www.preprints.org) | NOT PEER-REVIEWED | Posted: 22 December 2023 doi:10.20944/preprints202312.1709.v1

Table 3. ONC201 and harmaline (100 μM) mitochondrial toxicity in SH-SY-5Y and SK-N-AS spheroids performed by ATP assay after 72h of exposure to drugs. Data are expressed as mean ± SEM of three independent experiments (n = 3).

Drugs	SH-SY-5Y cell viability (%)	SK-N-AS cell viability (%)
ONC201	13.67 ± 6.23	17.5 ± 6.80
Harmaline	67.48 ± 13.91	44.24 ± 24.25

3.3. Harmaline and cell efflux pump interactions

The effectiveness of the drug is also related to its intracellular turnover which is mainly dependent on its activity towards the drug of the membrane efflux. It can be modified by the drug feature with respect to the membrane efflux pump, such as P-glycoprotein (P-gp). P-gp is an efflux protein present at the apical level of the BBB, responsible for the efflux of endogenous and exogenous ligands out from the CNS [34] and is considered as the BBB gatekeeper, our brain's first line of defense. Thus, to predict the ability of a drug to overcome the BBB and hit central targets measuring the interaction with P-gp is pivotal to be measured. A drug can be a substrate, modulator, or inhibitor of P-gp. Most known drugs are P-gp substrates. Three distinct biological assays are commonly used to evaluate the P-gp interacting mechanism: calcein-AM assay, ATP consumption, and the apparent permeability (Papp) determination.

Since calcein-AM is a pro-fluorescent probe and substrate of P-gp [51], it is effluxed from P-gp, remaining outside of cells that overexpress P-gp, such as BBB cells. When a compound interacts with P-gp, it can compete with the efflux of Calcein-AM, allowing the probe to enter cells, where it is hydrolyzed by cytoplasmic esterases into the fluorescent Calcein. Calcein, not being a substrate of P-gp and being hydrophilic, remains in the cell, giving a fluorescence signal. As evident from Table 4, no interaction was observed at the P-gp level for harmaline (EC_{50} > 100 μM), while a moderate interaction was observed for ONC201 (EC_{50} = 13.4 μM), while no interaction was observed at the P-gp level for harmaline (EC_{50} > 100 μM), potentially explaining the massive doses needed to produce effective action on patients. P-gp is ATP dependent, so its substrates result in cell depletion of ATP, while untransported compounds show an unchanged ATP cellular level. However, since we measured an interaction with P-gp but no associated consumption of ATP, we suggest that ONC201 could be included in the particular category of molecules interacting with P-gp which are defined as non-transported [52].

Table 4. Tested compounds efflux pumps activity and Apparent Permeability (P_{app}) values. Data are expressed as mean of three independent experiments, NT = Not Tested.

Drugs	P-gp EC_{50}, μM	ATP	P_{app}BA (nm/sec)	P_{app}AB (nm/sec)	BCRP EC_{50}, μM
ONC201	13.4	NO	2157	356	>100
Harmaline	>100	NT	2539	496	14.9

3.4. Biological membrane permeability by harmaline

The determination of P_{app} allows to establish the permeability of harmaline and ONC201 both in the basolateral-apical direction versus (P_{app}BA) and in the opposite direction (P_{app}AB). P_{app} is measured using a monolayer of the human colon carcinoma cell line (Caco-2 cells). This cell line endogenously expresses a variety of transporter proteins present in various endothelial and epithelial barriers of the body; in particular, it expresses the P-gp and BCRP efflux pumps present at the BBB [53]. Since Caco-2 cells express P-gp only apically, fluxes across the monolayer in the basolateral-apical direction (P_{app}BA) indicate passive transport. ONC201 and harmaline passively cross the membranes with a 2157 and 2539 nm/sec flux, respectively. Active mediated efflux is represented by

the $P_{app}AB$ value. The residual flow of ONC201 of 356 nm/sec is due to the fact that the drug is retained by P-gp (EC_{50} = 13.4μM). Harmaline $P_{app}AB$ is 496nm/sec but given its P-gp EC_{50} >100 μM, the possible interaction with another efflux pump normally expressed at the apical level (BCRP) was studied. Thus, BCRP activity for harmaline was measured, and its EC_{50} was found to be 14.9 μM.

4. Conclusions

This work arises from the need to identify new enhancers of *h*ClpP activity. Then, by FLAP, harmaline was identified as a compound with similar features to ONC201. The outcomes of molecular dynamics simulations demonstrated reduced stabilization in the harmaline binding site in contrast to ONC201; however, encouraging interactions between harmaline and *h*ClpP were still observed. Harmaline has been shown to be a moderate enhancer of *h*ClpP activity with moderate cytotoxic activity against both DIPG and neuroblastoma cells, which share the non-amplified MYCN gene, involved in tumor onset and progression. It was interesting to verify how harmaline crosses the blood-brain barrier through the combination of three *in vitro* tests, and this led to the hypothesis that the efflux pump involved in its transport is BCRP. The results will allow us to start research based on specific modifications of the harmaline chemical structure, which will lead to structure-activity relationships investigations aimed to identify compounds more potent than ONC201 and, therefore, capable to real contribute to fight DIPG.

Author Contributions: Conceptualization, A.S., M.G.P., C.G.F.; methodology, M.M., F.R. A.C., R.S., O.M.B, D.A., P.S., G.A, M.C. G.C., S.R., F.M.P; validation, M.M., P.L.P. C.G.F., M.G.P., A.S; investigation, M.M., M.G.P. A.S.; data curation, M.M., M.G.P., V.Z., S.F., E.C. A.S. All authors contributed to write the manuscript and have read and approved to the published version of the manuscript. All named authors meet the international criteria for authorship for this article, take responsibility for the integrity of the work, contribute to write this manuscript and have given their approval for this version to be published.

Funding: This research was funded by (a) the Ministry of Economic Development (MISE) funded project "GENESI" code 092-Prog n. F/180003/03/X43 for the development of innovative radiopharmaceuticals and biomarkers for the diagnosis of cancers of the male and female reproductive system (2021–2023); and (b) PRIN: progetti di ricerca di rilevante interesse nazionale –2022WYFST2

Institutional Review Board Statement: Not applicable.

Informed Consent Statement: Not applicable.

Data Availability Statement: Data is contained within the article.

Acknowledgments: The authors are grateful to Ahana Maitra@Stylus.inc. for linguistic revision. This work was supported by Associazione Progetto G.A.I.A., Onlus Mia Neri Foundation, Heal Foundation, Matibellula ODV.

Conflicts of Interest: All the authors declare no conflict of interest.

References

1. Perrone, MG, Ruggiero, A, Centonze, A, Carrieri, A, Ferorelli, F, Scilimati A. Diffuse Intrinsic Pontine Glioma (DIPG): breakthrough and clinical perspective. *Curr. Med. Chem.* **2021**, 28, 3287-3317.
2. Louis, D.N.; Perry, A.; Wesseling, P.; Brat, D.J.; Cree, I.A.; Figarella-Branger, D.; Hawkins, C.; Ng, H.K.; Pfister, S.M.; Reifenberger, G.; Soffietti, R.; von Deimling, A.; Ellison, D.W.; *Neuro Oncol.* **2021**, 23, 1231-1251.
3. Dalle Ore, C.; Coleman-Abadi, C.; Gupta, N.; Mueller, S. *Pediatr Neurosurg*. **2023**, Epub ahead of print.
4. Ralff, M.D.; Lulla, A.R.; Wagner, J.; El-Deiry, W.S. *Transl. Cancer Res.* **2017**, 6, S1239-S1243.
5. Wang, S.; Dougan, D.A. *Cancer Cell*. **2019**, 35, 707-708.
6. Wong, K.S.; Houry, W.A. *ACS Chem. Biol.* **2019**, 14, 2349-2360.
7. Cole, A.; Wang, Z.; Coyaud, E.; Voisin, V.; Gronda, M.; Jitkova, Y.; Mattson, R.; Hurren, R.; Babovic, S.; MacLean, N.; Restall, I; Wang, X.; Jeyaraju, D.V.; Sukhai, M.A.; Prabha, S.; Bashir, S.; Ramakrishnan, A.; Leung, E.; Qia, Y.H.; Zhang, N.; Combes, K.R.; Ketela, T.; Lin, F.; Houry,

W.A.; Aman, A.; Al-Awar, R.; Zheng, W.; Wienholds, E.; Xu, C.J.; Dick, J.; Wang, J.C.; Moffat, J.; Minden, M.D.; Eaves, C.J.; Bader, G.D.; Hao, Z.; Kornblau, S.M.; Raught, B.; Schimmer, A.D. *Cancer Cell.* **2015**, *27*, 864-876.

8. Feng, Y.; Nouri, K.; Schimmer, A.D. *Cancers.* **2021**, 13, 2020.
9. Keith, S.W.; Walid, A.H. *ACS Chem. Biol.* **2019**, 14, 2349-2360.
10. Böttcher, T.; Sieber, S. A. *Med Chem Comm*. **2012**, 3, 408.
11. Hackl, M.W.; Lakemeyer, M.; Dahmen, M.; Glaser, M.; Pahl, A.; Lorenz-Baath, K.; Menzel, T.; Sievers, S.; Bottcher, T.; Antes, I.; Waldmann H, Sieber SA. *J. Am. Chem. Soc.* **2015**, 137, 8475–8483.
12. Brötz-Oesterhelt, H.; Beyer, D.; Kroll, H.P.; Endermann, R.; Ladel, C.; Schroeder, W.; Hinzen, B.; Raddatz, S.; Paulsen, H.; Henninger, K.; Bandow, J.E.; Sahl, H-G.; Labischinski, H. Dysregulation of bacterial proteolytic machinery by a new class of antibiotics. *Nat. Med.,* **2005**, 11, 1082-1087.
13. Lee, B. G.; Park, E. Y.; Lee, K. E.; Jeon, H.; Sung, K. H.; Paulsen, H.; Rubsamen-Schaeff, H.; Brötz-Oesterhelt, H.; Song, H. K. *Nat. Struct. Mol. Biol.* **2010,** 17, 471-478.
14. Stahl, M.; Korotkov, V. S.; Balogh, D.; Kick, L. M.; Gersch, M.; Pahl, A.; Kielkowski, P.; Richter, K.; Schneider, S.; Sieber, S. A. *Angew. Chem.* **2018**, 57, 14602-14607.
15. Graves, P.R.; Aponte-Collazo, L.J.; Fennell, E.M.J.; Graves, A.C.; Hale, A.E.; Dicheva, N.; Herring, L.E.; Gilbert, T.S.K.; East, M.P.; McDonald, I.M.; Lockett, M.R.; Ashamalla, H.; Moorman, N.J.; Karanewsky, D.S.; Iwanowicz, E.J.; Holmuhamedov, E.; Graves, L.M. *ACS Chem Biol.* **2019,** 14, 1020-1029.
16. Ishizawa, J.; Zarabi, S.F.; Davis, R.E.; Halgas, O.; Nii, T.; Jitkova, Y.; Zhao, R.; St-Germain, J.; Heese, L.E.; Egan, G.; Ruvolo, V.R.; Barghout, S.H.; Nishida, Y.; Hurren, R.; Ma, W.; Gronda, M.; Link, T.; Wong, K.; Mabanglo, M.; Kojima, K.; Borthakur, G.; MacLean, N.; Ma, M.C.J.; Leber, A.B.; Minden, M.D.; Houry, W.; Kantarjian, H.; Stogniew, M.; Raught, B.; Pai, E.F.; Schimmer, A.D.; Andreeff, M. *Cancer Cell*, **2019**, 35, 721-737.
17. Madhukar, N.; Prabhu, V.V.; Anantharaman, L.; Sulli, C.; Davidson, E.; Deacon, S.; Tarapore, R.; Rucker, J.; Charter, N.; Doranz, B.; Oster, W.; Elemento, O.; Free, R.B.; Sibley, D.; Allen, J.E. *Neuro Oncol.* **2017**, 19, 81–82.
18. Carosati, E.; Sciabola, S.; Cruciani, G. *J. Med. Chem.* **2004**, 47, 5114-5125.
19. Jones, J.E.; Proc, R.; Soc; London; Lee, B.; Richards, F.M.; Jorgensen, E.C.; Connolly, M.L.; Ferrin, T.C.; Langridge, R.; Oatley, S.J.; Burridge, J.M.; Blake, C.C.F. *J. Med. Chem,* **1985**, 28-32.
20. Cheeseright, T., Mackey, M., Rose, S., & Vinter, A. Molecular field extrema as descriptors of biological activity: definition and validation. *J. Chem. Inf. Model.*, **2006**, 46(2), 665–676.
21. Bauer, M. R., & Mackey, M. D. Electrostatic Complementarity as a Fast and Effective Tool to Optimize Binding and Selectivity of Protein-Ligand Complexes. *J. Med. Chem.*, **2019**, 62(6), 3036–3050.
22. Case, D. A., Cheatham, T. E., 3rd, Darden, T., Gohlke, H., Luo, R., Merz, K. M., Jr, Onufriev, A., Simmerling, C., Wang, B., & Woods, R. J. The Amber biomolecular simulation programs. *J. Comput. Chem.* **2005**, 26(16), 1668-1688.
23. Salomon-Ferrer, R., Case, D.A., Walker, R. *WIREs Comput Mol Sci*, **2013**, 3: 198–210.
24. Wong, K.S.; Mabanglo, M.F.; Seraphim, T.V.; Mollica, A.; Mao, Y.-Q.; Rizzolo, K.; Leung, E.; Moutaoufik, M.T.; Hoell, L.; Phanse, S.; Goodreid, J.; Barbosa, L.R.S.; Ramos, C.H.I.; Babu, M.; Mennella, V.; Batey, R.A.; Schimmer, A.D.; Houry, W.A. *Cell Chem. Biol.* **2018**, 25, 1017-1030.
25. Iacopetta, D.; Madeo, M.; Tasco, G.; Carrisi, C.; Curcio, R.; Martello, E.; Casadio, R.; Capobianco, L.; Dolce, V. *Biochim. Biophys Acta* **2011**, 1807, 251-261.
26. Lunetti, P.; Cappello, A.R.; Marsano, R.M.; Pierri, C.L.; Carrisi, C.; Martello, E.; Caggese, C.; Dolce, V.; Capobianco, L. *Biochim Biophys Acta.* **2013,** 1827, 1245-1255.
27. See, Y.P.; Jackowski, G. *Protein Structure* (Creighton, T. E., ed.), IRL Press, Oxford; **1990.**
28. Tiwari, P.; Kaila, P.; Guptasarma, P. Electrophoresis. **2019**, 40, 1273-1281.
29. Corydon, T.J.; Bross, P.; Holst, H.U.; Neve, S.; Kristiansen, K.; Gregersen, N.; Bolund, L. *Biochem J.* **1998**, *331*, 309-316.
30. Kang, S.G.; Dimitrova, M.N.; Ortega, J.; Ginsburg, A.; Maurizi, M.R. *J Biol Chem*. **2005**, 280, 35424-35432.

31. Aziz-Bose, R.; Monje, M. *Curr Opin Oncol.* **2019**, 31, 522–530.
32. Grasso, C.S.; Tang, Y.; Truffaux, N.; Berlow, N.E.; Liu, L.; Debily, M.A.; Quist, M.J.; Davis, L.E.; Huang, E.C.; Woo, P.J.; Ponnuswami, A.; Chen, S.; Johung, T.B.; Sun, W.; Kogiso, M.; Du, Y.; Qi, L. Huang, Y.; Hütt-Cabezas, M.; Warren, K.E.; Le Dret, L.; Meltzer, P.S.; Mao, H.; Quezado, M.; van Vuurden, D.G., Abraham, J.; Fouladi, M.; Svalina, M.N.; Wang, N.; Hawkins, C.; Nazarian, J.; Alonso, M.M.; Raabe, E.H.; Hulleman, E.; Spellman, P.T.; Li, X.N.; Keller, C.; Pal, R.; Grill, J.; Monje, *M. Nat Med.* **2015**, 21, 555-559.
33. Qin, E.Y.; Cooper, D.D.; Abbott, K.L.; Lennon, J.; Nagaraja, S.; Mackay, A.; Jones, C.; Vogel, H. Jackson, P.K.; Monje, M. *Cell.* **2017,** 170, 845-859.
34. Contino, M.; Guglielmo, S.; Riganti, C.; Antonello, G.; Perrone, M.G.; Giampietro, R.; Rolando, B.; Fruttero, R.; Colabufo, N.A. *Eur. J. Med. Chem.* **2020**, 208, 112843-112864.
35. Braconi, L.; Dei, S.; Contino, M.; Riganti, C.; Bartolucci, G.; Manetti, D.; Romanelli, M.; Perrone, M.G.; Colabufo, N.A. Guglielmo, S.; Teodori, E. *Eur. J. Med. Chem.* **2023**, 259, 115716-115739.
36. Biondic, M.C.; Erra-Balsells, R. *J. Chem. Soc. Perkin trans. II*, **1992**, Issue 7.
37. Alijanpour, S.; Jafaripour, S.; Ghasemzadeh, Z.; Khakpai, F.; Zarrindast, M.R. *Eur. J. Pharmacol.* **2021**, 893, 173806-173812.
38. Mosaffa, S.; Ahmadi, H.; Khakpai, F.; Ebrahimi-Ghiri, M.; Zarrindast, M.R. P*sychopharmacology*, **2021**, 238, 259-269.
39. Zhao, T.; Ding, K.-M.; Zhang, L.; Cheng, X.-M.; Wang, C.-H.; Wang, Z.-T. *J. Chem.* **2013**, 2013, 1-6.
40. Herraiz, T.; Gonzalez, D.; Ancin-Azpilicueta, C.; Arán, V. J.; Guillén, H. *Food Chem. Toxicol*. **2010**, 48, 839-845.
41. Bensalem, S.; Soubhye, J.; Aldib, I.; Bournine, L.; Nguyen, A.T.; Vanhaeverbeek, M.; Rousseau, A.; Boudjeltia, K.Z.; Sarakbi, A.; Kauffmann, J.M.; Nève, J.; Prévost, M.; Stévigny, C.; Maiza-Benabdesselam, F.; Bedjou, F.; Van Antwerpen, P.; Duez, P. *J Ethnopharmacol*. **2014**, 154, 361-369.
42. Uddin, M.J.; Xu, S.; Crews, B.C.; Aleem, A.M.; Ghebreselasie, K.; Banerjee, S.; Marnett, L.J. *ACS Med Chem Lett.* **2020**, 11, 1881-1885.
43. Li, S.P.; Wang, Y.W.; Qi, S.L.; Zhang, Y.P., Deng, G.; Ding, W.Z.; Ma, C.; Lin, Q.Y.; Guan, H.D.; Liu, W., Cheng, X.M.; Wang, C.H. *Front Pharmacol*. **2019**, 24, 1430-1447.
44. Roy, S.; Mohammad, T.; Gupta, P.; Dahiya, R.; Parveen, S.; Luqman, S.; Hasan, G.M.; Hassan, M.I. *ACS Omega.* **2020**, 42, 27480–27491.
45. Rashidi, M.; Mahmoudian, E.; Mirzaei, S.; Mazloomi, S.N.; Bazi, A.; Azadeh, H.; Mozaffari, M. *Chem Biol Interact*. **2022,** 365, 1100871100.
46. Adnan, M.; Anwar, S.; DasGupta, D.; Patel, M.; Elasbali, A.M.; Alhassan, H.H.; Shafie, A.; Siddiqui, A.J.; Bardakci, F.; Snoussi, M.; Hassan, M.I. *Int J Biol Macromol*. **2023,** 224, 188-195.
47. Hashemi, S.; Shabani, S.; Rabiei, Z.; Enferadi, S.T.; Vannozzi G.P; *Biotechnol Rep* **2015**, 8, 138-143.
48. Jackson, E.R.; Persson, M.L.; Fish, C.J.; Findlay, I.J.; Mueller, S.; Nazarian, J.; Hulleman, E.; van der Lugt, J.; Duchatel, R.J.; Dun, M.D. *Neuro Oncol.* **2023**, 17, 144-152.
49. Zingales, V.; Torriero, N.; Zanella, L.; Fernández-Franzón, M.; Ruiz, M.J., Esposito, M.R.; Cimetta, E. *Food Chem. Toxicol.* **2021**, 157, 112605-112619.
50. Mahringer, A.; Fricker, G. *Expert Opin. Drug Metab. Toxicol.* **2016**, 12, 499- 508.
51. Orlický, J.; Sulová, Z.; Dovinová, I; Fiala, R;. Zahradníková, A. Jr.; Breier, A. *Gen Physiol Biophys*. **2004**, 23, 357-66.
52. Remigijus, D.; Pranas J.; Alex A.; Alanas P.; *J Drug Target* **2003**, 11, 391-406.
53. Chatterjee, S.; Deshpande, A.A.; Shen, H. *Biopharm Drug Dispos.* **2023**, 44, 7-25.